Site-specific order and magnetism in tetragonal Mn$_3$Ga thin films

Karsten Rode,[*] Nadjib Baadji, Davide Betto, Yong-Chang Lau, Hüseyin Kurt,[†] M. Venkatesan,
Plamen Stamenov, Stefano Sanvito, and J. M. D. Coey
CRANN and School of Physics, Trinity College Dublin, Dublin 2, Ireland

Emiliano Fonda, Edwige Otero, Fadi Choueikani, and Philippe Ohresser
Synchrotron SOLEIL, L'Orme des Merisiers Saint-Aubin, 91192 Gif-sur-Yvette Cedex, France

Florence Porcher and Gilles André
Laboratoire Léon Brillouin, UMR12 CEA-CNRS, 91191 Gif-sur-Yvette Cedex, France

Mn$_3$Ga bulk material and thin films deposited on several different substrates have been investigated using x-ray and neutron diffraction, x-ray absorption spectroscopy, x-ray magnetic circular dichroism, and electronic structure calculations using density-functional theory with the aim of determining the atomic site occupancy, magnetic moments, and magnetic structure of this tetragonal D0$_{22}$-structure compound. The Mn$_3$Ga has close to ideal site occupancy, with Ga on $2a$ sites and Mn on $2b$ and $4d$ sites. The magnetic structure is basically ferrimagnetic, with the larger Mn moment of about 3 μ_B on the $2b$ site, which is coordinated by 8 Mn $4d$ and 4 Ga, and the smaller one on the $4d$ site, which is coordinated by 4 Mn $2b$, 4 Ga, and 4 Mn $4d$. The Mn d-band occupancy is close to 5 on both sites, and the orbital moments are small, <0.2 μ_B. The material nevertheless exhibits substantial uniaxial anisotropy, $K_u = 1.0$ MJ m^{-3}, which originates from the $4d$ site. The $2b$ site has hard axis anisotropy, which together with an oscillatory exchange coupling from the first and second nearest neighbors, leads to a soft component of the magnetization in the c plane, coexisting with c-axis hysteresis loops exhibiting coercivity of up to 1.2 T, and magnetization in the range 110–220 kA m^{-1} at room temperature, depending on preparation conditions. Tetragonal Mn$_2$Ga films behave similarly. Manganese is lost from both sites, but the films have substantially larger magnetization (480 kA m^{-1}) and anisotropy constant (2.35 MJ m^{-3}) than Mn$_3$Ga.

PACS number(s): 75.25.−j, 75.30.Gw, 75.50.Vv

I. INTRODUCTION

Highly anisotropic, ferromagnetic, metallic materials are important building blocks for future applications in high-density magnetic storage and logic due to their inherent hysteretic magnetic stability. At present, the most often used material combination for achieving high on-off ratios (magnetoresistance, MR) is the CoFeB/MgO/CoFeB trilayer.[1] These tunnel junctions can provide MR above 200% at room temperature thanks not solely to the spin polarization of the electrodes, but also to the $\vec{k}$-dependent transmission of the CoFe electron wave through the MgO barrier.[2,3] There are, however, several improvements possible to this solution. Firstly, the industry-compatible growth of such stacks is only possible by the deposition of MgO on the amorphous CoFeB layer, followed by a subsequent annealing at ∼350 °C in order to crystallize the CoFeB by driving the boron out to a nearby getter such as Ta. Cubic CoFe is a material with rather weak magnetic anisotropy and hence thermal stability is usually achieved by exploiting the, weak, shape anisotropy of the structure. Stacks with in-plane magnetization are not scalable to the 10-nm node. The scaling problem can potentially be solved by sandwiching ultrathin CoFeB between MgO and Ta as the resulting magnetic layer has uniaxial, perpendicular anisotropy due to the weak interface anisotropy that becomes dominant.[4–6]

Another limitation of that system is the difficulty of integration of any other multifunctional material from the oxide family. It has been proved difficult to use, for example, SrTiO$_3$ as a barrier due to lattice mismatch.

There has recently been a revived interest in the intermetallic compounds from the Heusler alloy family. This interest is due to the extremely varied physical properties that can be found within this class of materials.[7] Alloys showing ferromagnetism and ferrimagnetism are readily obtained both in bulk and thin film forms. Furthermore, semiconducting[8] and insulating materials can also be synthesized, as well as materials with more exotic properties like superconductors and topological insulators.[9,10] Half-metallic Heusler alloys are useful in magnetic tunnel junctions and spin valves but the high spin polarization[11–14] of these materials was only demonstrated at low temperatures, although moderately high TMR can be maintained at room temperature.

Of special interest are the tetragonally distorted Heusler alloys. While the cubic L2$_1$ Heusler alloys are virtually isotropic, their tetragonal cousins can display very high uniaxial magnetic anisotropy coupled with tunable saturation magnetization and high spin polarization. This is especially true in the case of D0$_{22}$ Mn$_3$Ga.[15–18] Thin films of this material exhibit high, perpendicular, uniaxial anisotropy and grow with ease on both MgO and SrTiO$_3$ substrates, as well as a number of lattice matched seed layers like Cr and Pt.

In this paper, we focus on the structural and magnetic properties of the tetragonally distorted Heusler alloy Mn$_3$Ga. The macroscopic magnetic properties of both the thin-film samples on a variety of substrates and seed layers, as well as the bulk powder, are first investigated. We then use synchrotron radiation to record local order and occupation ratios as well as site-specific magnetic properties. In particular,

we highlight the noncollinear magnetic structure in Mn_3Ga evidenced by neutron diffraction and make estimates of the direction and magnitude of the orbital moments on each crystallographic site. Finally, we compare our experimental findings with density functional theory (DFT) calculations of the electronic structure and magnetic properties of the $D0_{22}$-structure Mn_3Ga.

II. EXPERIMENTAL DETAILS

We have grown thin-film samples of $Mn_{3-x}Ga$ on 10×10 mm^2 (001)-oriented $SrTiO_3$ and MgO single-crystal substrates using a "Shamrock" fully automated deposition tool. The films were sputtered from stoichiometric Mn_3Ga, Mn_2Ga, and Mn targets onto substrates at a temperature of 350 °C. The samples were then capped with ∼5-nm MgO. The nominal thickness of the $Mn_{3-x}Ga$ was 60 nm. Prior to further investigation, the actual thickness of the samples was determined by low-angle x-ray reflectivity. In the case of the intermediate stoichiometry, $Mn_{2.5}Ga$, the samples were produced by co-sputtering from the Mn_2Ga target and the Mn target. Therefore the Mn to Ga ratio is well-known (and verified by inductively coupled plasma mass spectroscopy) in the cases of Mn_3Ga and Mn_2Ga, but it is likely different from the nominal $Mn_{2.5}Ga$ composition in the co-sputtered case.

The crystal structure and lattice parameters were determined by symmetrical and reciprocal space map scans using a BRUKER D8 diffractometer. The primary optics used were a Cu K_α x-ray tube, a Göbel mirror, and a double-bounce channel-cut Ge crystal monochromator. A 0.1-mm divergence slit and a 2.5° Soller slit were used for the final beam conditioning. On the diffracted beam side, a 1D "LynxEye" detector and a 2.5° Soller slits were used.

The macroscopic magnetic properties were measured with a Quantum Design superconducting quantum interference device (SQUID)-based magnetometer, using the reciprocating sample option (RSO) and linear regression-based data reduction. We also recorded the magnetization using a physical properties measurement system (PPMS) system with a vibrating sample magnetometer (VSM) insert from the same supplier. The maximum applied magnetic field is $\mu_0 H = 5.0$ and 14.0 T, respectively.

Extended x-ray absorption fine structure (EXAFS) at the Mn and Ga K edges was recorded at room and liquid nitrogen temperatures on the SAMBA beamline[19] at the SOLEIL synchrotron, France (proposal number 20110285) using fluorescence detectors (Vortex50 from SIINTUSA). X-ray absorption spectroscopy (XAS) on the Mn $L_{2,3}$ edges was carried out at the same synchrotron facility on the DEIMOS beamline (proposal No. 20120494) with both circular left and right polarizations in order to measure the x-ray magnetic circular dichroism (XMCD). These measurements were all carried out at room temperature, with the applied magnetic field either parallel or perpendicular to the wave vector $\vec{k}$. We measured XMCD by first saturating the sample as far as possible by applying 5 T perpendicular to the sample surface in the positive direction, then we reduced the applied magnetic field to 100 mT and measured absorption for both photon helicities. Next, we reversed the magnetization by applying

−5 T, followed by the application of the measurement field, −100 mT. The measurements for the case where $\mu_0 \vec{H} \perp \vec{k}$ were carried out in the same fashion but with the measurement field of ±100 mT applied in the orthogonal direction.

We furthermore synthesized bulk powders of Mn_3Ga by arc melting the appropriate amounts of Mn and Ga in an Ar atmosphere followed by an anneal at 400 °C for 7 days. The annealed ingots were then crushed in a stainless steel mortar. The resulting powder is coarse-grained and unsuitable for accurate powder x-ray diffraction. Neutron diffraction, on the other hand, offers a good contrast between Mn and Ga, and direct access to the long-range magnetic structure.

We measured neutron diffraction on the Mn_3Ga crushed powders on the 3T2 instrument (Laboratoire Léon Brillouin, Orphée neutron source) using a short wavelength of 1.2256 Å over a Q range of 0.42 to 8.9 $Å^{-1}$.

III. STRUCTURAL AND MAGNETIC PROPERTIES

We focus on the site-specific magnetic and structural properties of Mn_3Ga thin films grown on $SrTiO_3$ substrates. In order to make a consistent analysis of the results, it is necessary to understand as far as possible, the macroscopic magnetic and structural properties of these films in relation to thin-film samples grown on different substrates/seed layers as well as the bulk powders. Further details regarding the growth and characterization of thin films on MgO and on seed layers of Pt and Cr are published elsewhere.[15,16]

Mn_3Ga crystallizes in the $D0_{22}$ structure, space group number 139, $I4/mmm$ with Mn in two nonequivalent sites, Wyckoff positions $2b$ and $4d$ while Ga occupies the $2a$ position. Mn spins in the $2b$ positions couple ferromagnetically to each other and antiferromagnetically to those of Mn in the $4d$ position. The overall magnetic structure is therefore expected to be a collinear ferrimagnet with alternating planes of up ($4d$) and down ($2b$) moments, with both sites having their spins aligned with the crystallographic c axis.

In Fig. 1, we plot the $2\theta - \theta$ x-ray diffraction diagrams of three thin films of $Mn_{3-x}Ga$ on $SrTiO_3$ and two films grown directly on MgO. Both series of samples show a high degree of texturing with the c axis parallel to the growth direction. Reciprocal space mapping and ϕ scans reveal that both series show in-plane order with the Mn_3Ga [100] in-plane direction parallel to the $SrTiO_3$ and MgO [100] directions. As can be seen from the displacement of the reflection at $2\theta \sim 52°$, the lattice c parameter is decreasing with increasing Mn content. We also recorded reciprocal space maps (RSM) around the [116] reflection of $Mn_{3-x}Ga$ to determine the in-plane lattice parameter a. A summary of the structural parameters of a selection of samples on various seed layers and compositions is given in Table I.

As outlined above, the $Mn_{2.5}Ga$ samples are denoted by their nominal composition. The actual composition depends on the sputtering yields of the Mn_2Ga and Mn targets. Using Vegard's law, and taking the lattice parameters for Mn_3Ga and Mn_2Ga as the solid solution end members, we can estimate the actual composition of the $Mn_{2.5}Ga$ sample grown on $SrTiO_3$ to be $Mn_{2.77}Ga$.

The $D0_{22}$ structure, illustrated in Fig. 2, differs from the $L1_0$ structure by the ordering of Mn and Ga in the Wyckoff $2b$
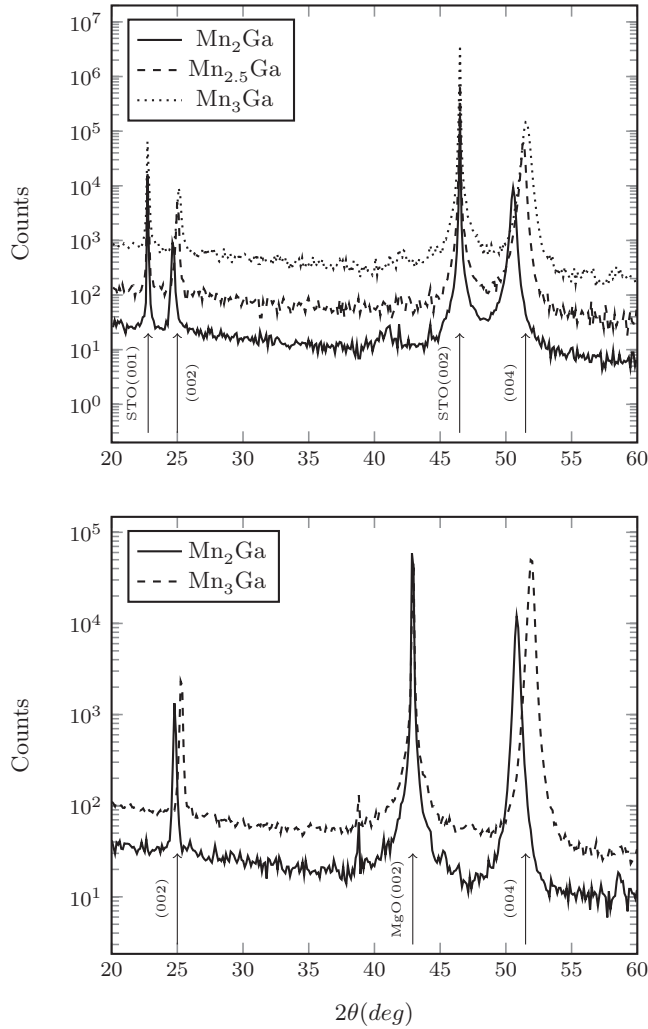
FIG. 1. X-ray diffraction of $Mn_{3-x}Ga$ films on $SrTiO_3$ (top) and on MgO (bottom) substrates. The curves are offset for clarity.
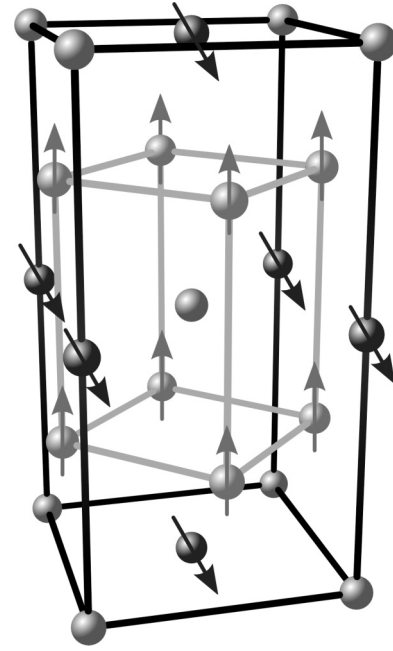

FIG. 2. The $D0_{22}$ crystal structure. Mn in the $4d$ position in light grey and Mn in the $2b$ position in dark grey, both with arrows indicating the direction of the magnetic moments on each site. Ga in the $2a$ position is represented by light grey and no arrow. In the perfectly ordered crystal, the central atom in the unit cell is always Ga.

and $2a$ positions, respectively. In the case where the central atom in the unit cell can be either Ga or Mn, the symmetry of the unit cell is changed. This leads to a unit cell where the a lattice parameter is unaltered, but the c parameter is half that of the $D0_{22}$ structure. If this disorder is complete, this material has a c/a ratio >1, leading to easy-axis anisotropy.[20,21] In the case of a partially ordered $D0_{22}$-like structure, the ratio $c/2a$ is <1, suggesting that such disorder should favour an easy-plane magnetocrystalline anisotropy. A measure of the degree of $2a-2b$ order is obtained by recording the integrated intensities of the x-ray diffraction [101] and [204] peaks and normalising to the theoretical value of this ratio: the order parameter is $S = \sqrt{(I_{101}^{obs}/I_{204}^{obs})/(I_{101}^{cal}/I_{204}^{cal})}$. We find that at higher values of the order parameter, the ratio between the in-plane and the out-of-plane saturation moments increases, indicating that the noncollinearity of the magnetic structure in

TABLE I. Summary of macroscopic parameters with different samples identified by their substrate (and seed layer). We show lattice parameters a and c, the structural order parameter S and the saturation magnetization $M_{S\perp}$. The in-plane value $M_{s\parallel}$ is defined as the saturation of the soft part of the curve, obtained by extrapolating the linear slope of the high-field magnetization.

Composition	Substrate/seed	a^a (Å)	c^a (Å)	c^b (Å)	S^c	$M_{s\perp}$ (kA m^{-1})	$M_{s\parallel}$ (kA m^{-1})	$M_{s\parallel}/M_{s\perp}$ (%)
Mn_3Ga	$SrTiO_3$	3.92	7.08	7.0852	0.56	155	6	3.87
$Mn_{2.5}Ga$	$SrTiO_3$	3.91	7.12	7.1124	n/a	315	5	1.59
Mn_2Ga	$SrTiO_3$	3.91	7.22	7.2134	0.21	430	10	2.33
Mn_3Ga	MgO	3.92	7.04	7.0345	0.68	217	15	6.91
Mn_2Ga	MgO	3.92	7.17	7.1781	n/a	440	30	6.82
Mn_3Ga	MgO/Pt	3.91	7.06	7.0622	0.71	111	21	18.9
Mn_3Ga	MgO/Cr	n/a	n/a	6.9363	n/a	140	0	0

[a]From reciprocal space mapping.

[b]From symmetrical $2\theta-\theta$ scans.

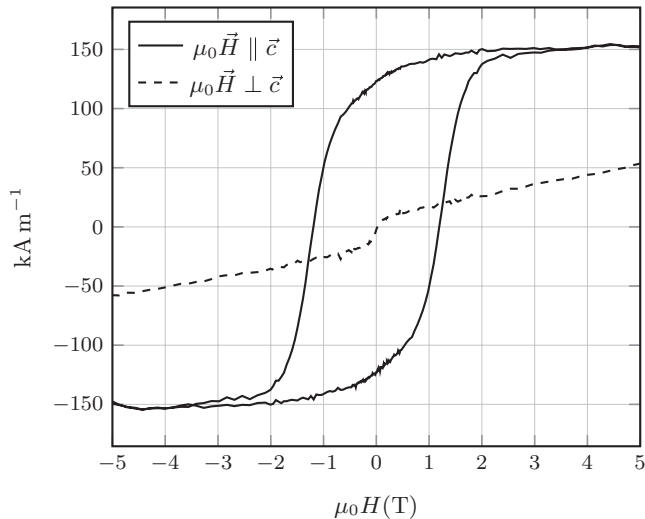[c]S is the $2a-2b$ order parameter, defined in the text.

FIG. 3. SQUID magnetometry of a Mn_3Ga thin-film sample on $SrTiO_3$ at 300 K. The $\mu_0 \vec{H} \perp \vec{c}$ loop shows a small in-plane moment.
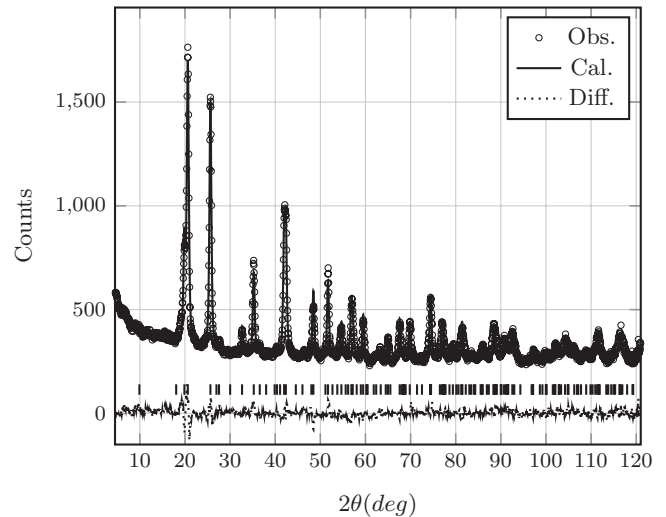

FIG. 4. Neutron diffraction pattern of Mn_3Ga bulk powder. The figure shows the observed intensities as a function of the scattering angle, as well as the refined fit, the difference, and the Bragg positions.

Mn_3Ga is not due to disorder. This is particularly obvious in the case of the bulk powders of Mn_3Ga where the Rietveld refinements of the nuclear and magnetic structures converge to good R values with no need for substitutional Mn on the Ga position or vice versa (see Sec. III A1). When the disorder is complete over all three sites, the structure becomes face-centred cubic.

In Fig. 3, we plot the hysteresis loops of Mn_3Ga on $SrTiO_3$ with the magnetic field applied perpendicular ($\mu_0 \vec{H} \parallel \vec{c}$) and parallel ($\mu_0 \vec{H} \perp \vec{c}$) to the film surface. The strong magnetocrystalline anisotropy is obvious from the coercive field of ~1.2 T. The anisotropy field obtained by extrapolating the in-plane loop to the saturation magnetization is $\mu_0 H_a = 15$ T, corresponding to a uniaxial anisotropy energy of 1.1 MJ m^{-3}. A small, soft, in-plane component of the magnetization is clearly visible. We are confident this contribution is not due to a secondary phase, but is rather an intrinsic property of the $Mn_{3-x}Ga$ alloys in the $D0_{22}$ structure because it is not seen when the field is applied perpendicular to the plane. A randomly oriented secondary phase with a soft moment should have been observed in either of the two applied field orientations. This is not the case. A perfectly oriented phase with an easy-plane, hard-axis anisotropy may be responsible for this behavior, but in that case (a phase with almost perfect crystalline texture and occupying ~10% of the sample) we should have been able to detect it in the symmetric x-ray diffraction scans. Hence the more likely origin is that the in-plane moment is an intrinsic property of partially disordered $D0_{22}$ $Mn_{3-x}Ga$. In Mn_3Ga, a magnetic moment of 1 μ_B f.u.$^{-1}$ (formula unit) (2 μ_B per unit cell) corresponds to a magnetization of 170 kA m^{-1}. The values of the c-axis magnetization on Table I range from 0.6 to 1.3 μ_B f.u.$^{-1}$.

A. Bulk powders of Mn_3Ga

1. Neutron diffraction

In Fig. 4, we plot the Mn_3Ga neutron diffraction diagram recorded at room temperature. As the magnetic ordering temperature of Mn_3Ga is above the temperature where the material

undergoes a structural transformation from the tetragonal $D0_{22}$ to the hexagonal $D0_{19}$ structure, we cannot measure above the magnetic ordering temperature to obtain a purely nuclear diffraction pattern. While the nuclear form factor is constant in 2θ (and Q) space due to the fact that the scatterers are point charges, the magnetic form factor is similar to the x-ray form factor and decreases quickly at high values of 2θ. The large Q range accessible on 3T2 facilitates the decorrelation of the magnetic and structural information.

We made a Rietveld refinement of the neutron diffraction diagram and obtain a good agreement with the experimental data, although a minor secondary phase is present. This is apparent in the lower angular range. We constrained the magnetic contribution so that the magnetization along the c axis is in agreement with the magnetometery measured on the same sample using a VSM (see Sec. III A2). The refinement is shown in Fig. 4 and the structural and magnetic properties obtained are summarized in Table II. The refinement yields a Bragg R factor of 7.42 for the nuclear part and a magnetic R factor of 2.69.

As expected from the discussion above, we find that there is a significant in-plane moment carried by the Mn atoms in the Wyckoff 2b position. In the case of our Mn_3Ga bulk powder, it corresponds to a tilt of the 2b moments of 21° from the crystallographic c axis.

2. High-field magnetization of partially ordered powders

We measured the magnetic properties of the bulk Mn_3Ga powder to obtain a reference point for both the saturation magnetization and the anisotropy. In randomly oriented powders,

TABLE II. Mn_3Ga neutron Rietveld refinement parameters. We show lattice parameters a and c, as well as the magnetic moments carried by Mn in the 4d and 2b positions.

a (Å)	c (Å)	m_z^{4d} (μ_B/Mn)	m_z^{2b} (μ_B/Mn)	m_x^{2b} (μ_B/Mn)
3.9056(2)	7.1003(6)	2.08(2)	−3.07(4)	1.19(24)

the saturation magnetization and the anisotropy field can be obtained from a fit of the approach to saturation.

The Mn_3Ga crushed powder was diluted in a two-component polymer glue and left to set in a 5-T applied field in order to induce as much texture as possible in the sample. This attempt to induce texture was only partially successful, most probably due to the coarse nature of the powder—every grain is composed of several crystallites of Mn_3Ga, each with a random orientation. We obtain a saturation magnetization of 180 kA m^{-1}(1.1 μ_B f.u.$^{-1}$). The apparent anisotropy energy assuming perfect crystalline texture is $K_{app} = 0.13$ MJ m^{-3}, leading to a uniaxial anisotropy energy K_u of 1.0 MJ m^{-3}.

B. Local order and magnetism of Mn_3Ga thin films

The possibility of a noncollinear magnetic structure with quite different anisotropy energies on the two magnetic sublattices is uncommon. In order to elucidate the origin of this behavior, we have carried out a detailed analysis of both the structural and magnetic properties of Mn_3Ga thin films, using EXAFS and XAS/XMCD.

1. EXAFS

We recorded EXAFS spectra on the Ga and Mn K edges at room temperature and at liquid nitrogen temperature. At low temperature, we obtained a much higher signal-to-noise ratio and hence the following results and discussion are based on the low-temperature data. Furthermore, we recorded spectra at each edge with the linear polarization of the incoming x-rays making an angle of 78° ($\vec{E} \perp \vec{c}$) and 22° with the crystal $\vec{c}$ axis ($\vec{E} \parallel \vec{c}$). Using the FEFF[22,23] code to calculate a theoretical model from the ideal, perfectly ordered D0$_{22}$ structure, we simultaneously fitted the two edges with both polarizations to confirm that the local order is in agreement with that structure. The observed bond lengths are given in Table III.

The choice of a structural model is more complicated in the case of Mn_2Ga as we have no *a priori* knowledge of which site, $4d$ or $2b$, that will preferentially loose occupancy. Fitting the first coordination shell on the EXAFS signal for both polarizations at the Ga K edge and assuming negligible Ga vacancies, we found that Mn vacancies are distributed over $2b$ and $4d$ sites with a occupancy of 0.56(4) and 0.72(2), respectively. Based on this result, it is possible to build a structural model and calculate the EXAFS signal for both edges and polarizations. Visual inspection confirmed that Mn is equally lost in both sites and that multiple scattering paths corroborate this hypothesis. The bond lengths for Mn_2Ga are reproduced in the lower part of Table III. The recorded spectra at the Ga and Mn edges for both polarizations are shown in Fig. 5, along with the fitted curves.

2. Site-specific magnetic properties

We have seen that thin films of Mn_3Ga grown on MgO and $SrTiO_3$ substrates, differ from the simple magnetic model of alternating, antiferromagnetically coupled planes. The neutron diffraction analysis points to an in-plane moment carried by the $2b$ Mn and the SQUID magnetometry confirms a magnetically soft in-plane component. This noncollinear magnetic mode,

TABLE III. Bond lengths and σ^2 for Mn_3Ga and Mn_2Ga on MgO. The occupancy of each site is set to 100% in the case of Mn_3Ga and to 75% $4d$ and 50% $2b$ occupancy in the Mn_2Ga case. The atoms are identified by their Wyckoff positions, i.e., Mn in $2b$ and $4d$. Ga in $2a$.

Edge(polarization) Mn_3Ga	Path	R (Å)	σ^2 (10^{-3} Å^2)
Ga($\vec{E} \perp \vec{c}$)	$4d$-$4d$/$2b$-$2a$	2.755(8)	2.9(8)
	$4d$-$2b$/$4d$-$2a$	2.619(7)	1.9(7)
Ga($\vec{E} \parallel \vec{c}$)	$4d$-$4d$/$2b$-$2a$	–	–
	$4d$-$2b$/$4d$-$2a$	2.623(7)	3.8(9)
Mn($\vec{E} \perp \vec{c}$)	$4d$-$4d$/$2b$-$2a$	2.764(5)	2.3(6)
	$4d$-$2b$/$4d$-$2a$	2.631(5)	3.3(5)
Mn($\vec{E} \parallel \vec{c}$)	$4d$-$4d$/$2b$-$2a$	–	–
	$4d$-$2b$/$4d$-$2a$	2.637(5)	2.9(5)
Mn_2Ga			
Ga($\vec{E} \perp \vec{c}$)	$4d$-$4d$/$2b$-$2a$	2.75(1)	4(1)
	$4d$-$2b$/$4d$-$2a$	2.629(8)	2.6(5)
Ga($\vec{E} \parallel \vec{c}$)	$4d$-$4d$/$2b$-$2a$	–	–
	$4d$-$2b$/$4d$-$2a$	2.643(6)	2.8(4)
Mn($\vec{E} \perp \vec{c}$)	$4d$-$4d$/$2b$-$2a$	2.757(9)	1.9(8)
	$4d$-$2b$/$4d$-$2a$	2.652(7)	2.9(7)
Mn($\vec{E} \parallel \vec{c}$)	$4d$-$4d$/$2b$-$2a$	–	–
	$4d$-$2b$/$4d$-$2a$	2.662(7)	3.1(7)

where the anisotropy seen by the two different sites is of opposite sign is most unusual.

The magnetocrystalline anisotropy is reflected in the variation of the orbital moment when magnetized along the easy and hard axis. Transition metal L-edge soft x-ray spectroscopy and dichroism is a tool particularly suited to investigate this magnetic mode as it allows for the independent determination of both the spin and the orbital moment. If furthermore, the two sites had been chemically different, the determination of the site-specific properties would have been as simple as tuning the incoming x-ray energy to the appropriate edge. Our case is a bit more intricate, as Mn is occupying both the $2b$ and $4d$ positions. Another complication of our measurement is that the accurate determination of the spin moment is dependent on a clear separation between the L_3 and the L_2 multiplet manifolds. This is the case when the core-hole $2p$ spin-orbit coupling is sufficiently high, as in Fe and Co but in the case of Mn this is not necessarily the case. We will see from the experimental data that there is some overlap between the two. We have chosen to fix an energy value, which we define as the end of the L_3 and start of the L_2 edges. In this fashion, while the absolute value of the spin moment may be over or underestimated, the error is completely systematic.

It has been suggested that the tetragonal distortion of the L2$_1$ Heusler structure to the D0$_{22}$ variant is due to Jahn-Teller distortion created by Mn$-d^4$ ions.[24] In Fig. 6, we compare the pre-edge of four different Mn-containing materials, Mn_3Ga, MnO, MnO_2, and Mn-metal. If Mn in Mn_3Ga was present in the Jahn-Teller-active configuration d^4, we should expect to observe the absorption edge shift towards the ionic compounds MnO and MnO_2. This is not the case, so we conclude that the tetragonal distortion in the case of Mn_3Ga is not due to Jahn-Teller-active charge configuration of the manganese. The
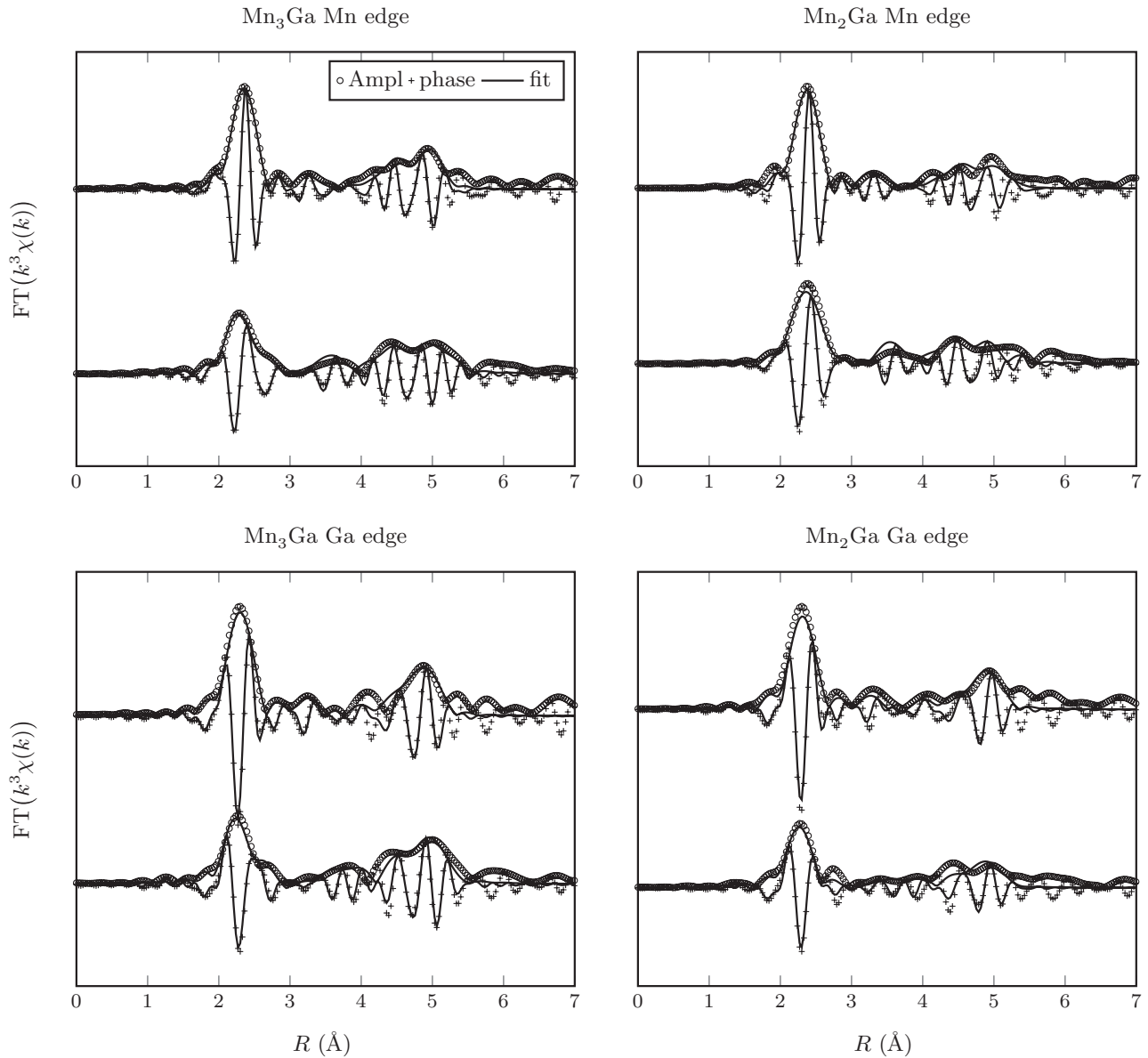
FIG. 5. Moduli and imaginary (marks) parts of the Fourier transformed EXAFS signals at both Mn and Ga edges. Each panel contains the Fourier transforms of the EXAFS data and the corresponding FEFF model (solid lines, see text). Within each panel, the upper manifold corresponds to $\vec{E} \perp \vec{c}$ and the lower to $\vec{E} \parallel \vec{c}$.

absorption edge of Mn_3Ga is almost overlapping with that of Mn metal, indicating a strong degree of delocalization of the d-band electrons. In this case, the minimization of energy will take place through participation in the chemical bonds rather than by Jahn-Teller distortion. It is furthermore known that although some Mn-containing Heusler alloys do tetragonally distort, this is not generally true;[25] there are also examples of Heusler alloys containing no Mn, which exhibit a tetragonal distortion, such as Ni_2TiGa.[26]

In Fig. 7, we present the spin moments and their angles with respect to our choice of coordinate system for both the case where the applied magnetic field is parallel to ($\vec{H}_\parallel$) and perpendicular to ($\vec{H}_\perp$) the propagation vector $\vec{k}$ of the x-ray beam. In the figure, ϕ is the angle between the sample normal and $\vec{k}$, while θ is the angle between the spin moments

on each site. In the case of a collinear arrangement of the spins, $\theta = 180°$. The magnitude of the magnetic field applied during measurement is $\mu_0 H = 100$ mT, too weak to reverse the magnetization of the sample, as can be seen from Fig. 3. The soft, in-plane, component does, however, follow the applied magnetic field. We will see in Sec. IV B that the anisotropy energy associated with the $4d$ position is one order of magnitude higher and of opposite sign, compared to the $2b$ one. While the $4d$ Mn is easy axis, the $2b$ is easy plane, so we conclude that in the measurement field, only the direction of the Mn-$2b$ spin moment is changing. As it can be seen from the figure, the projection of the $4d$ spin moment on the propagation vector depends only on the angle between the sample normal and $\vec{k}$, while the projection of the $2b$ spin moment depends on both ϕ and θ, and is different depending on whether the
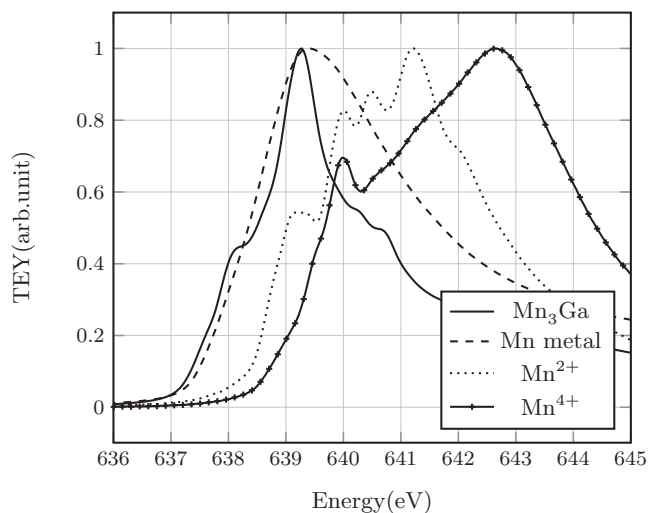
FIG. 6. Comparison of the Mn XAS L_3 pre-edge of Mn in Mn_3Ga, Mn^{2+}(MnO), Mn^{4+}(MnO$_2$) and Mn-metal.

applied field is perpendicular or parallel to $\vec{k}$. The measured magnitude of $\langle S \rangle$ as a function of the angle ϕ can then be written as

$$S_{\vec{H}\parallel}(\phi) = S^{4d} \cos(\phi) + S^{2b} \cos(\phi - \theta) \qquad (1)$$

and

$$S_{\vec{H}\perp}(\phi) = S^{4d} \cos(\phi) + S^{2b} \cos(\phi + \theta). \qquad (2)$$

The sum rules[27–29] allow the independent determination of $\langle L \rangle$ and $\langle S \rangle_{\text{eff}} = \langle S \rangle + 7/2\langle T \rangle$ where $\langle L \rangle$ and $\langle S \rangle$ are the expectation values for the orbital and spin operators, respectively, and $\langle T \rangle$ is the expectation value for the magnetic dipole operator. In the transition metal series, $\langle T \rangle$ is usually much smaller than both $\langle L \rangle$ and $\langle S \rangle$. We made a numerical estimate of the energy of the dipole interaction in Mn_3Ga and found that it corresponds to an energy $\sim 1 \, \text{kJ} \, \text{m}^{-3}$, or about 0.1% of the total measured anisotropy energy. For the
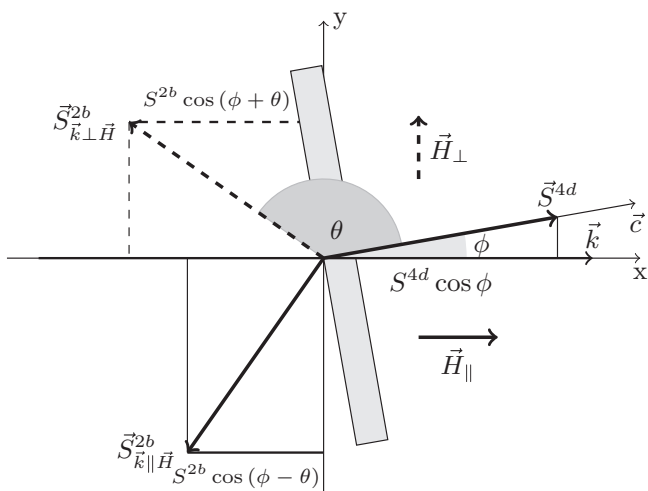

FIG. 7. Experimental setup for the XAS and XMCD measurements and definitions of the angles. The thin-film sample is represented as a grey rectangle.
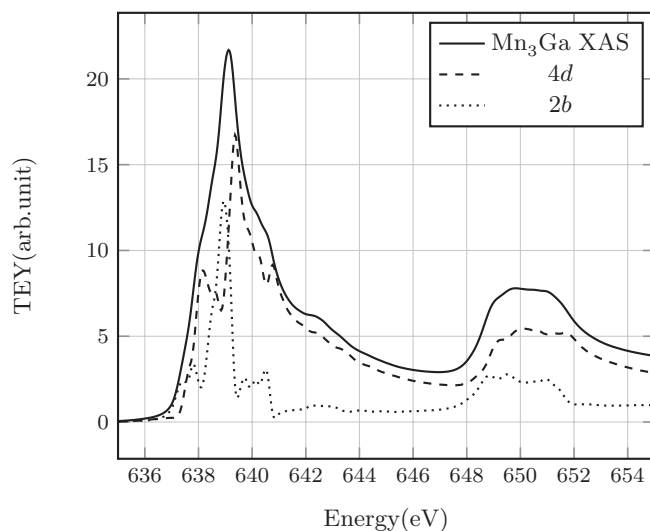

FIG. 8. The x-ray absorption spectrum of Mn_3Ga at the $L_{2,3}$ edges and the contributions from the $4d$ and $2b$ sites obtained by the site decomposition as described in the text.

reminder of this paper, we will assume that $\langle S \rangle_{\text{eff}} = \langle S \rangle$. The number of holes in the Mn^{3d} band can be deduced from our calculations (see Sec. IV below); we find that Mn in the $4d$ and $2b$ positions have 4.82 and 4.90 holes/Mn, respectively. The $3d$ band is therefore almost half-full.

We recorded XAS for both circular polarizations at more than eight different incidence angles ϕ in the two magnetic field configurations on samples Mn_2Ga, $Mn_{2.5}Ga$, and Mn_3Ga. Representative XAS and XMCD spectra are shown in Figs. 8 and 9, respectively.

The difference between the two magnetic configurations discussed above allows us to estimate the contribution from each site. The system of two equations [see Eqs. (1) and (2) above] has, however, three unknowns: $\langle S \rangle^{4d}$, $\langle S \rangle^{2b}$, and θ. Our knowledge of the occupation ratio for the two Mn positions, obtained from the EXAFS measurements described above,
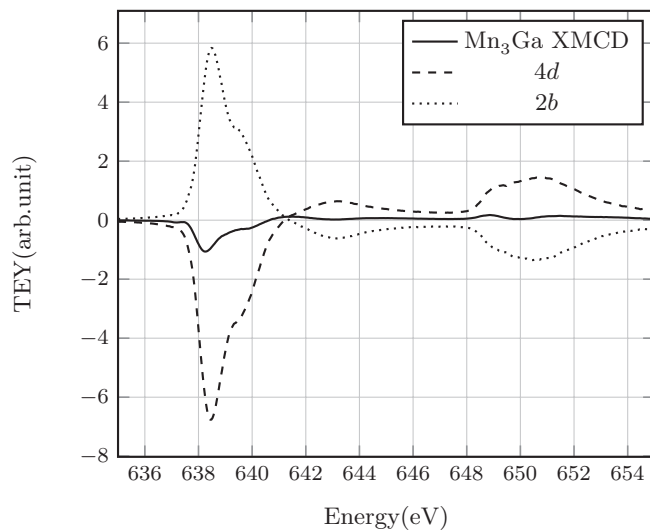

FIG. 9. The x-ray magnetic dichroism spectrum of Mn_3Ga at the $L_{2,3}$ edges and the contributions from the $4d$ and $2b$ sites obtained by the site decomposition as described in the text.
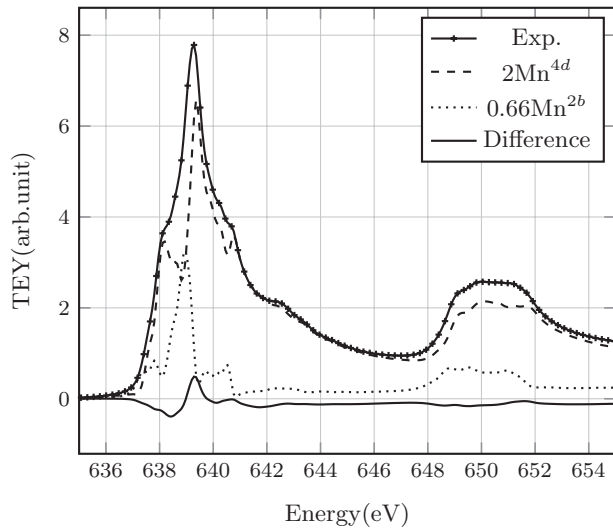
FIG. 10. The $Mn_{2.5}Ga$ experimental XAS and the simulation using the extracted contribution from the $4d$ and $2b$ sites.

FIG. 11. The $Mn_{2.5}Ga$ experimental XMCD and the simulation using the extracted contribution from the $4d$ and $2b$ sites.

makes it possible to decompose the spectra into $2b$ and $4d$ contributions. In order to do so, we must make sure that each spectrum on each sample corresponds to the same number of Mn atoms. The data reduction procedure was the following: (1) we normalized pre-edge to 1; (2) we calculated the sample total $\langle S \rangle$ and $\langle L \rangle$ by applying the sum rules; (3) we subtracted 1 from the scans and normalized post-edge to 1 thereafter; (4) by subtracting, using appropriate factors, Mn_2Ga spectra from Mn_3Ga, we obtained site-specific XAS for each helicity and angle; (5) we calculated site-specific values of $\langle S \rangle$ and $\langle L \rangle$.

The separation of the XAS and associated XMCD into site-specific spectra using the methods outlined above, may introduce errors in the values of both $\langle S \rangle$ and $\langle L \rangle$, in particular, if the $2p \rightarrow CB$ (conduction band) absorption differs from one sample to the next. This is not our case, and we believe that the errors introduced using this method is less than the overall error associated with the application of the sum rules. An experimental verification of the procedure can be obtained from the simulation of the $Mn_{2.5}Ga$ XAS and XMCD spectra. We know from Sec. III that analysis of the x-ray diffraction diagrams of this sample indicates that its real stoichiometry is closer to $Mn_{2.77}Ga$. We used a least-square simultaneous fitting of the XAS and XMCD data of the sample using the extracted $2b$ and $4d$ contributions. In Figs. 10 and 11, we show the results of these fits. The agreement with the experimentally observed absorption and XMCD is reasonably good. We find from the fit that the $Mn_{2.5}Ga$ sample has composition $Mn_2Mn_{0.66}Ga$, or in other words, a fully occupied $4d$ site and a 66% occupied $2b$ site. The slight difference—2.77 against 2.66—may be due to the different modification of the lattice parameter depending on if the loss of Mn is primarily on the $4d$ or $2b$ positions. If we base a similar analysis on the magnetization, comparing the measured macroscopic magnetization with the measured magnetic moment at each site (see below), we find $Mn_2Mn_{0.73}Ga$.

In Figs. 12 and 13, we plot the measured spin moment of the Mn_3Ga sample. In Fig. 12, the data points are obtained by applying directly the sum rules to the experimental spectra. In Fig. 13, we have carried out the decomposition of each
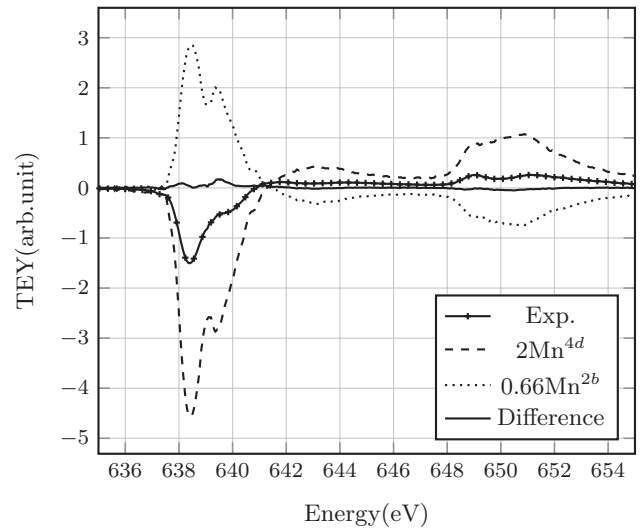
XAS spectrum as described above, and then the XMCD was calculated for each pair of helicities. We chose to use the two data sets presented in Fig. 12 and the data set relative to the Mn $4d$ from Fig. 13 for the simultaneous fitting using the appropriate cosine-dependent functions. The result of the fit is plotted as solid lines in the figures. We find a Mn-$4d$ and $2b$ spin moment of 2.67(2) μ_B and 4.74(5) μ_B, respectively, giving a net moment of 0.6 μ_B f.u.$^{-1}$. The angle between the two spins is found to be $179.5(5)°$.

We now turn to the orbital moment. As can be expected from the number of holes in the $3d$ band, the orbital contribution to the magnetic moment is very small. Indeed, for an ion in a spherical symmetry, with $n_h = 5$, we expect the orbital moment to be exactly zero. Furthermore, as it is the case with transition metals, the $3d$ bands in Mn_3Ga are contributing to
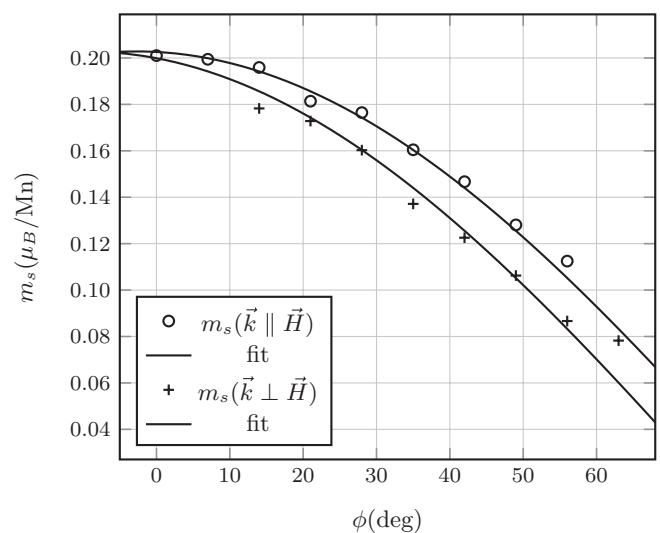

FIG. 12. Total spin moment for Mn_3Ga with the applied magnetic field parallel and perpendicular to the wave vector $\vec{k}$. The experimental values have been extracted from the spectra using the sum rules directly on the recorded spectra. The lines are simultaneous fits to the data in this figure and the $4d$ contribution shown in Fig. 13.
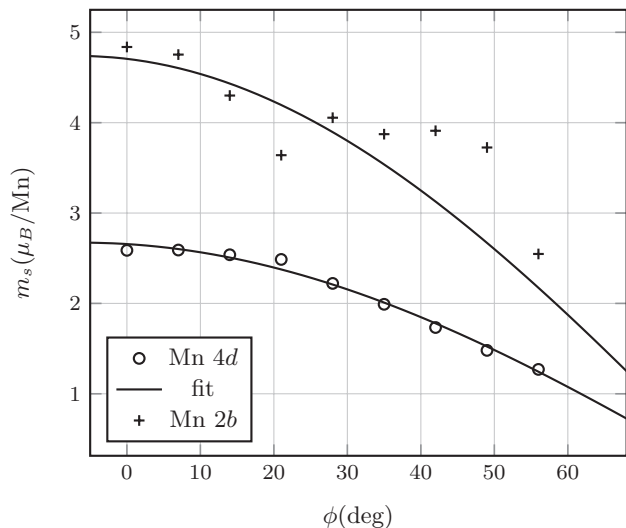
FIG. 13. Absolute value of the sample spin moment (μ_B/Mn) deconvoluted to the two Mn positions, $4d$ and $2b$. The solid line relative to the $2b$ moments is a guide to the eye, while the line relative to the $4d$ moments is a simultaneous fit using this data set and the two data sets presented in Fig. 12.

the chemical bonding, so that the orbital moment is quenched, because of crystal averaging, even in lower symmetries.

In Fig. 14, we plot the site-specific orbital moments as a function of the angle between the wave vector $\vec{k}$ and the sample normal. Despite the poor signal-to-noise ratio, due to the very low magnitudes, we can make an estimate of the orbital moments and their direction with respect to the sample normal, the crystallographic c axis, coinciding with the spin direction of the Mn $4d$ ions. We find that the Mn in positions $4d$ and $2b$ carry 0.05 μ_B, 0.12 μ_B and make angles of 38°, 235°, respectively. These values are obtained using the methodology for separation of the sites described above. As previously mentioned, this may introduce small errors in the
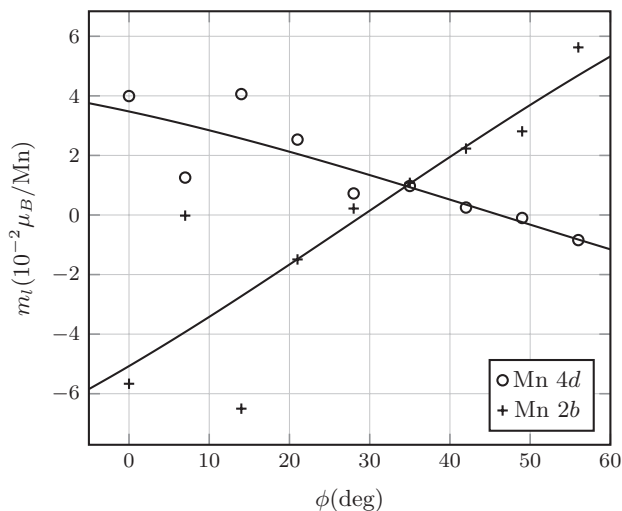

FIG. 14. Site-specific orbital moments in Mn$_3$Ga. The solid lines, obtained by fitting the data with a cosine to account for the angular projection of the orbital moment on $\vec{k}$, allow us to determine the magnitude of the orbital moment at each Mn position.
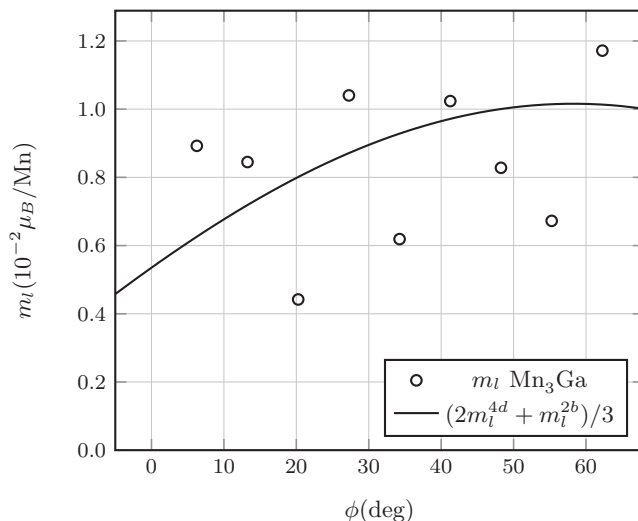

FIG. 15. Mn$_3$Ga total orbital moment derived directly from the sum rules. The solid line corresponds to the sum of the site-specific orbital moments as shown in Fig. 14.

derived expectation values for $\langle S \rangle$ and $\langle L \rangle$. While $\langle S \rangle$ is big enough to make it reasonable to ignore this source of error, it is clearly not the case for the orbital moment. In Fig. 15, we plot the measured total orbital moment using the sum rules directly on the recorded spectra, and compare it to the sum of the site-specific orbital moments shown in Fig. 14. The agreement between the two methods is very reasonable, in view of the magnitude of the signal.

The orbital moments were all measured in the configuration where the applied magnetic field is parallel to the propagation vector $\vec{k}$. The magnetocrystalline anisotropy will ensure that the magnitude of the orbital moments changes when the field is applied perpendicular to the easy axis, i.e., $\vec{H} \perp \vec{k}$. In this configuration, the signal-to-noise ratio is too poor to be able to extract the orbital moments, and a further experiment where one can to saturate the magnetization along the hard direction is necessary in order to obtain direct evidence of the magnitude of the anisotropy. We estimate from the site-specific data, that in the $\vec{H} \perp \vec{k}$ case, the orbital moment on the $4d$ Mn is decreasing by approximately 0.02 μ_B, while it is increasing by 0.03 μ_B on the $2b$ Mn. This indicates that the two sites have different sign of the anisotropy energy, and that while Mn in the $4d$ position has easy-axis anisotropy, the $2b$ position on the contrary has easy-plane anisotropy.

The experimentally observed magnetic structure is summarized in Fig. 16. We find, in agreement with the SQUID magnetometry, that the total magnetic moment is about 0.2 μ_B/Mn, or 0.6 μ_B f.u.$^{-1}$. Furthermore, in agreement with the calculated filling of the d bands of Mn at the two positions (more than half-filled), $\vec{L} \cdot \vec{S} > 0$. We also find evidence for a noncollinear structure, although this is much less obvious in the thin films grown on SrTiO$_3$ than it is in the bulk powders, or indeed in thin films grown on MgO or on a Pt seed layer (see Table I). The anisotropy of the orbital moment, and hence the magnetocrystalline anisotropy indicates easy-axis behavior for the $4d$ Mn, while it indicates, on the contrary, an easy-plane for the $2b$ Mn.
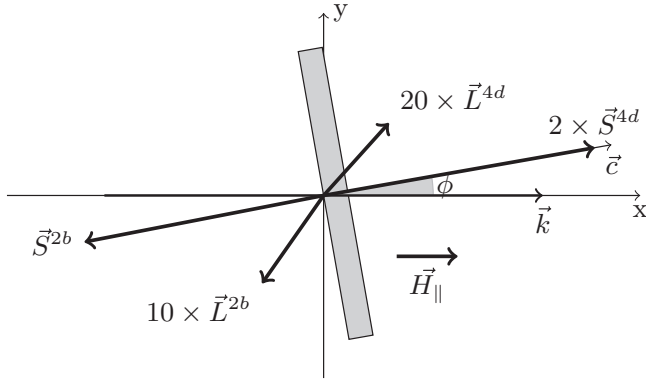
FIG. 16. Experimentally observed, site-specific, magnetic structure of Mn_3Ga. The figure is to scale, noting that the $4d$ $\vec{S}$ and $\vec{L}$ have been multiplied by 2 and 20, respectively, and the $2b$ $\vec{L}$ by 10.

IV. THEORY

To calculate XMCD and XAS spectra, the electronic structure of $Mn_{3-x}Ga$ was obtained using the full-potential linearized augmented plane-wave method[30,31] as implemented in the FLEUR code.[32] Spin-orbit coupling was included in the self-consistent calculations as described in Ref. 33 and the generalized gradient approximation (GGA)[34] was adopted for the exchange-correlation parametrization. XMCD was implemented as in Refs. 35 and 36. The experimental lattice parameters were used here, including the fractional coordinates as verified by the EXAFS study. The convergence was checked versus the number of k points. A muffin-tin radius of 2.44 a.u. was used for Mn and Ga. Inside these spheres, the basis set was expanded on lattice harmonics up to $l = 10$. In the interstitial region, 1478 symmetrized plane waves were used to expand the charge density and the full potential, while for the wave function, we took $k_{max} = 4.0$ a.u.$^{-1}$.

A. Spin and orbital moments

In Fig. 17, we show the calculated atomic contribution to the XAS, compared to experimentally extracted spectra at the L_3 edge. The agreement at this edge is fair, but the L_3/L_2 intensity ratio is substantially different (not shown). This ratio is around 2 for the theoretical spectra, as expected for a much reduced orbital moment, whilst the experimental data show a ratio between 3 and 4. In addition, the L_2 edge is much broader than the L_3 one, due to the different lifetimes of the excited states associated with each core state. A Gaussian convolution ($\sigma = 0.1$ eV) is used for the theoretical spectra. The $2p$ spin-orbit splitting of the cores states is accurately reproduced by the calculation. The calculated value of the $3d$ spin-orbit coupling strength $\lambda = 59$ and 57 meV for $4d$ and $2b$, respectively. The spin-orbit interaction is $\lambda \vec{L} \cdot \vec{S}$.

In Table IV, we report the calculated values for both the spin and orbital momentum for the different Mn sites and we compare them with the experimental values both from XMCD and neutron scattering. The agreement between theory and experiments is good overall; we find that the spin moment at the $4d$ site is well reproduced by our calculations, although there is a difference between the XMCD-measured spin moment at the $2b$ site compared to both theory and neutron diffraction.
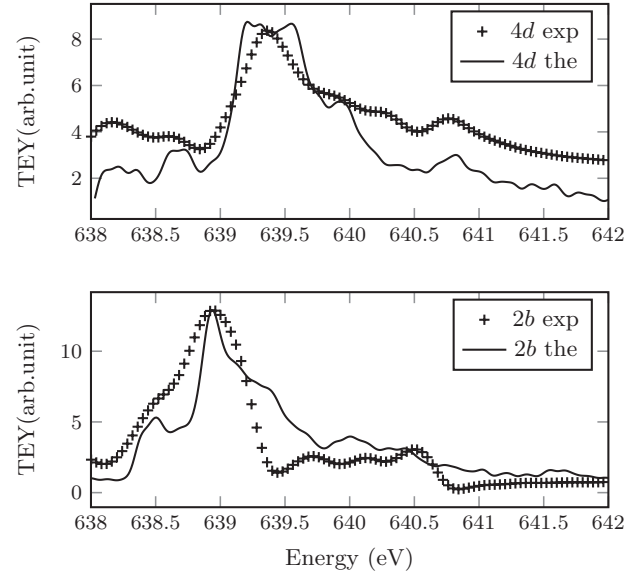

FIG. 17. Mn_3Ga experimental XAS deconvoluted to each crystallographic position, compared to the theoretically calculated spectra.

However, the values obtained by XMCD are strongly affected by how we separate the L_2 edge from the L_3 edge when using the sum rules. A closer agreement could be obtained by changing the energy that separate these two contributions. Furthermore, the difference between the experimental value for the orbital and spin moments and the calculated ones, is associated with the big difference in the L_2 edge spectra. It may also be related to electron correlation, that some authors suggest to be underestimated in local density approximation for such Heusler alloys.[18] However, the energy position of the peaks at the L_3 edge is well reproduced by the GGA approach, meaning that it is well suited to describe the electronic structure of Mn_3Ga (within the DFT framework). In addition, the sign of the projection of the orbital moment on the spin moment ($\vec{L} \cdot \vec{S}$) is positive for both sites and is confirmed by both theory and experiment. The positive sign of $\vec{L} \cdot \vec{S}$ indicates that the d orbitals of the Mn atoms at both sites ($2b$ and $4d$) are more than half-filled, and the value of $\langle L \rangle$ is proportional to the number of electrons above half-filling ($N_e - 5$). We find in the calculations that the number of electrons is approximately 5.10 and 5.18 for the $3d$ shell of Mn $2b$ and $4d$ atoms, respectively.

To conclude this section, we remark that the theoretical data presented here are all obtained at the experimental lattice

TABLE IV. Observed spin and orbital moments for Mn_3Ga, measured by XMCD and neutron diffraction (ND), $\langle L \rangle / \langle S \rangle$ ratio and the angle between $\vec{L}$ and $\vec{S}$, compared to the calculated (DFT) values.

Site		$2\langle S \rangle$	$\langle L_\parallel \rangle$	$\langle L \rangle / \langle S \rangle$	$\angle \vec{L}, \vec{S}$ (deg)
$2b$	XMCD	-4.74	-0.12	0.022	55
	ND	-3.29			
	DFT	-3.22	-0.014	0.004	$-7.3(15)$
$4d$	XMCD	2.67	0.048	0.018	38
	ND	2.08			
	DFT	2.54	0.020	0.008	1.8(3)

parameters. Full geometry optimization at the GGA level gives $a = 3.77$ Å and $c = 7.108$ Å ($c/a = 1.885$), slightly underestimating a, while accurately reproducing c. When compared to the calculations of Kübler,[37] we find that a agrees well with his value but our c is slightly smaller. However, the magnetic properties change little with such small variations in lattice parameters; when recalculated at the optimized lattice values, the magnetic moments are 2.85 and 2.33 for the $2b$ and $4d$ sites, respectively.

B. Magnetic anisotropy

We now calculate the magnetic anisotropy Δ defined as $\Delta = E(S \parallel [100]) - E(S \parallel [001])$, where E is the difference of total energy of the systems calculated self-consistently, for each quantification axis (SCF), including the spin-orbit term $H = H_0 + \sum_i \lambda_i \vec{L} \cdot \vec{S}$, where the sum is over the atoms in the unit cell and $\lambda_i = \frac{e}{4m^2} \frac{1}{r} \frac{dV_i}{dr}$ with V_i being the spherical part of the potential inside the atomic muffin-tin i. Alternatively, it can be calculated from the sum of the occupied eigenvalues using the force theorem.[38,39] The presence of two nonequivalent types of Mn in the $D0_{22}$ ($2b$ and $4d$) leads to a different contribution of each atom to the magnetic anisotropy, which we have considered by putting $\lambda_i = 0$ for different cases. For the case Δ all the atom contributions are considered together, for Δ_{2a} only the λ of the Ga is nonzero, for Δ_{2b} only λ of Mn $2b$ is nonzero, and for Δ_{4d} only that of Mn $4d$ is nonzero.

From Table V, we can see that the spin-orbit coupling tends to align Mn-$2b$ magnetization in plane ($\Delta < 0$), while the Mn $4d$ aligns more strongly along the axis. Due to the strong exchange coupling ΔE_{ex}, calculated to be of the order of 400 meV (see Fig. 18), and the fact that the magnetic anisotropy for $4d$ sites is much larger than that of $2b$, both spins lie along the c axis. The Mn $2b$ magnetization is calculated to be misaligned from the c axis by less than a degree, $\theta < 1°$ (where $\cos \theta = \Delta_{2b}/\Delta E_{\text{ex}}$) and even with a variation of $\langle L \rangle$ by 0.1 μ_B, the angle is increased only to about $3°$. The exchange interaction and the spin-orbit coupling can account for a maximum angle between the magnetization of the $4d$
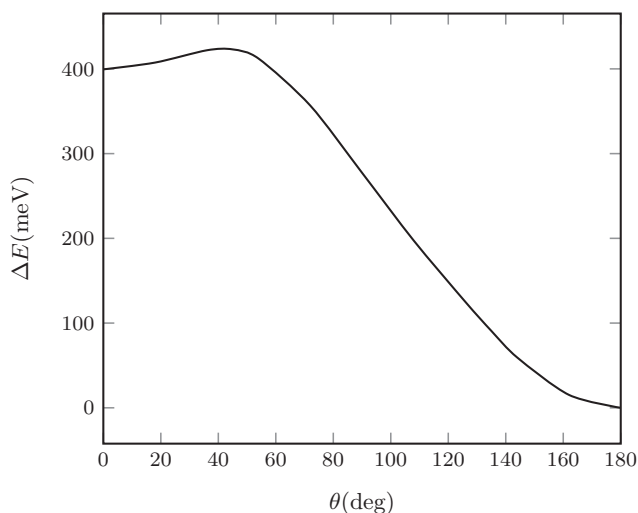
and $2b$ sites of a few degrees. The large angle observed in bulk neutron diffraction, and in thin-film samples grown on Pt or MgO, indicates a noncollinear ground state, which can be achieved if the exchange interaction between spins changes sign and forces a more complicated magnetic structure. In the next section, we will discuss how the exchange parameter could change in Mn_3Ga.

C. Exchange coupling from non-nearest neighbors

Manganese-containing alloys, starting with Mn itself, are known to exhibit a rich variety of magnetic order. The order in α-Mn metal is a complex noncollinear antiferromagnetism.[40] The noncollinearity is mainly due to a competition between ferromagnetic and antiferromagnetic couplings between nearest and more distant neighbors. We will show that in the case of Mn_3Ga, the exchange coupling J, changes sign from positive for the nearest neighbors (ferromagnetic) to negative for the next nearest ones. This oscillatory coupling continues at longer distances, but with rapidly decaying amplitude (see Fig. 19).

Our DFT calculation within the GGA was able to reproduce the experimentally observed absorption and dichroism spectra, hence we use the same formalism to evaluate the sign and magnitude of the exchange coupling. The magnetic excitations in an itinerant-electron system can be described either by Stoner, or spin wave excitations (magnons). At low temperature, the Stoner excitations can be neglected compared to the magnons. We use the frozen-magnons approximation and the total energy for the spin-spiral calculations is mapped onto a classical Heisenberg model, $E = -\sum_{i \neq j, R} J_{ij}(R) S_i(0) S_j(R)$, where i, j are the magnetic indices in the unit cell at $R = 0$ and R is the position of the Rth cell. J_{ij} are Heisenberg exchange parameters.

The Heisenberg exchange parameters are calculated using 2304 k points and $7 \times 7 \times 9$ q points. The magnetic moments inside the muffin-tin spheres are constrained to their noncollinear ground-state values. The results are shown in Fig. 19.
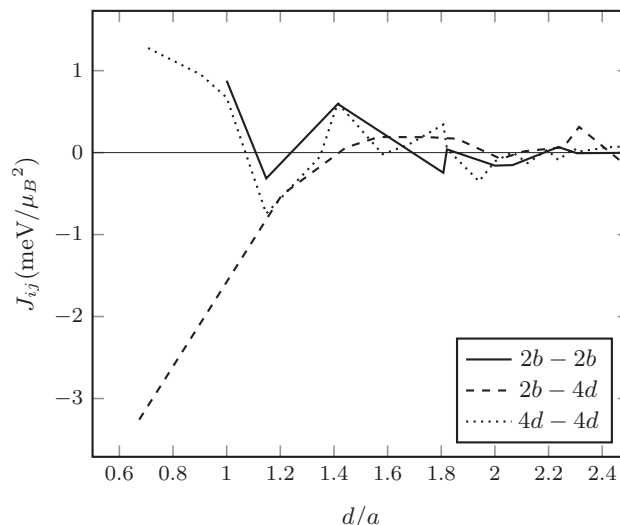

FIG. 18. Variation of the total energy as function of the angle between the Mn $2b$ and Mn $4d$.

FIG. 19. Calculated magnitude of the exchange parameter J_{ij} as a function of the reduced distance d/a for the three magnetic interactions.

TABLE V. Calculated magnetic anisotropy in meV (MJ m^{-3}) using self-consistent (SCF) and force theorem calculations for Mn_3Ga where different contributions are taken into account: (Δ) all atoms contribute, (Δ_{2a}) only Ga atoms, (Δ_{2b}) only Mn $2b$ atoms and (Δ_{4d}) only Mn $4d$ atoms contribute to the anisotropy.

	Δ	Δ_{2a}	Δ_{2b}	Δ_{4d}
SCF	0.899 (2.650)	0.021 (0.062)	-0.031 (-0.091)	0.765 (2.255)
Force theorem	0.900 (2.653)	0.022 (0.065)	-0.030 (-0.088)	0.765 (2.255)

We find that, for Mn $2b$, while the nearest neighbors couple ferromagnetically with an exchange parameter $J = 0.88$ meV μ_B^{-2}, the second nearest neighbor contribute with an antiferromagnetic coupling, -0.31 meV μ_B^{-2}. These competing couplings signify that in order to minimize the total energy of the system, the magnetic moments will adopt a noncollinear state. However, for Mn $4d$, the first three nearest neighbors are coupled ferromagnetically with relatively strong $J = 1.27$, 0.95, and 0.67 meV μ_B^{-2}. The fourth nearest neighbors are coupled antiferromagnetically with $J = -0.74$ meV μ_B^{-2}. This makes the Mn-$4d$ magnetic order less frustrated than the Mn $2b$. As a result, we have a frustrated ferrimagnet where the moments on at least one of the two Mn sites will tilt with respect to the high symmetry c axis. The anisotropy energy on the $4d$ position is higher by about a factor 10 than the one associated to the $2b$ position (see Table V). Furthermore, we find that while the $4d$ position has a easy-axis configuration, the $2b$ is an easy-plane one. Hence, the total magnetic energy, sum of the spin-orbit and exchange energies, favors a tilt of the spin in the $2b$ Mn site, in agreement with our experimental observations, both in thin films of Mn_3Ga on $SrTiO_3$ and MgO/Pt substrates, and in bulk powders of the same material.

The spin spiral DFT calculation allows us to determine the magnon dispersion spectrum (see Fig. 20) from which we deduce the spin stiffness, as the curvature of the dispersion. It is straightforward then to obtain a theoretical value for the Curie temperature. The calculated spin stiffness for a planar configuration is 559 meV Å^2, corresponding to an RPA[37] Curie temperature of 670 K. This value is slightly smaller than that of Kübler.[37] The difference between the two calculated values
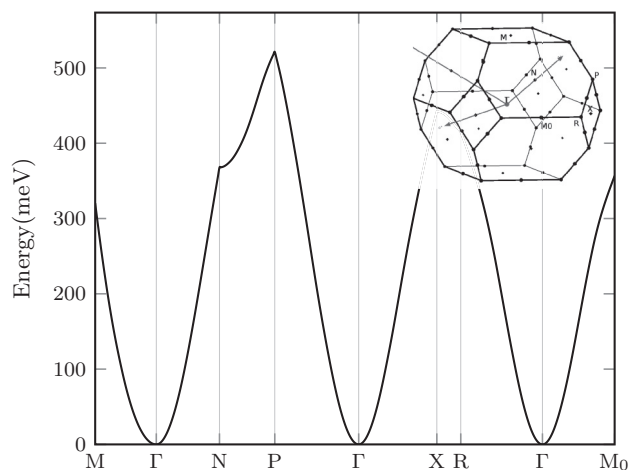
is probably due to the different lattice parameters considered in the calculations.

We finally want to comment on the internal magnetic structure, i.e., on the relative orientation of the spin and orbital moments at the two sites. From Table IV, we note that both theory and experiments confirm the noncollinear structure, but they disagree significantly on the angle between spin and orbital moments. Noncollinearity is forbidden by the symmetry of the crystallographic unit cell but it is permitted in the magnetic cell, which has $P1$ rather than $P4$ symmetry. The disagreement between theory and experiment we attribute to the small value of the orbital moment, which introduces a significant error into the estimate. Crucially, the qualitative features—sign of $\vec{L} \cdot \vec{S}$ and sign of anisotropy—are well described.

V. DISCUSSION

We have experimentally demonstrated that it is possible to use XAS and XMCD to investigate the magnetic structure of a complex system—Mn_3Ga. The deconvolution of the XAS/XMCD spectra into site-specific subspectra allows us to determine the ground-state values of $\langle S \rangle$ and $\langle L \rangle$ for each site. As expected for ions with close to half-filling of the d band, the orbital moment is close to zero. Nevertheless, we are able to make good estimates for their values, both when the applied magnetic field is parallel or perpendicular to the easy magnetic axis. From this, we can build up a qualitative picture of the nature of the anisotropy on each site. While the Mn in the $4d$ sites is highly anisotropic with an easy c axis, the $2b$ position exhibits perpendicular to c anisotropy. The strong uniaxial anisotropy in the $4d$ position and the strong, antiferromagnetic exchange between $4d$ and $2b$ positions yields the highly anisotropic ferrimagnetic ground state. This picture is confirmed by DFT calculations. We successfully reproduce the experimental XAS spectra for each site, which confirms that the theoretical model we have chosen is appropriate to describe Mn_3Ga.

The experimental observations and the theoretical calculations agree on a magnetic structure where the moments on the two Mn sites, are not collinear. From the experimental point of view, this is most obvious in bulk powders and in thin films grown on a Pt seed layer, samples that have the highest degree of $2a - 2b$ order. Insight into the origin of this in-plane magnetization from GGA-DFT is that the exchange coupling in the case of Mn_3Ga, is oscillating between ferro and antiferromagnetic values, and we show that this will lead to a noncollinear arrangement of the spin moments in Mn_3Ga.

FIG. 20. Magnon dispersion for Mn_3Ga. The inset illustrates the directions in reciprocal space.

The ratio of the net in-plane to out-of-plane saturation magnetization varies from 0% to 19% in the thin-film samples to almost 50% in the bulk powder. The degree of magnetic frustration depends on the ratio between the ferromagnetic and antiferromagnetic exchange couplings, which depend mainly on the distances between the magnetic ions and will therefore change when the lattice parameters or the site occupancies change. In our thin film and bulk powder samples, the a lattice constant is more or less constant, but the c parameter varies by as much as $\sim$5%. The effective distance also depends, to a much greater extent, on the atomic-scale (dis)order of the sample. In our opinion, the latter origin is the main reason for the variation of the magnitude of the in-plane component of the magnetization from sample to sample. The degree of frustration is proportional to the ratio between the second nearest neighbor antiferromagnetic coupling to the first nearest neighbor ferromagnetic one. $2a - 2b$ disorder increases the first nearest neighbor ferromagnetic coupling by a factor of almost 2, and reduces the frustration by the same amount. This leads to a more collinear magnetic order.

This unusual magnetic configuration in Mn_3Ga is interesting from a fundamental point of view, and could be of potential use in device physics. The in-plane moment adds a new handle to control the reversal process in magnetic recording materials, for example. While a high uniaxial anisotropy is required to obtain long-term thermal stability, the write process is hindered by the fact that a conventional ferromagnet, in the monodomain configuration, will reverse under an applied field equal to the anisotropy field, $2K_1/M_s$. In the case of $Mn_{3-x}Ga$, the reversal will be assisted by the in-plane moment, providing a means to tilt the magnetization away from the easy axis and increase the instability under an anti parallel magnetic field much more effectively than thermal variation is able to.

Another interesting possibility is spin injection. Injecting spins into a system with two opposing anisotropies, where one is perpendicular to the other may provide a way to obtain high spin-torque efficiency. This could be useful not only for spin transfer torque driven magnetic random access memory, but also in the generation of high frequency spin-torque oscillations.

VI. CONCLUSION

The site-specific magnetic properties of Mn_3Ga have been investigated both experimentally and theoretically. Although there are some variations between samples and between the results of different measurements, the overall picture is clear. The tetragonal Heusler-type compound is a ferrimagnetic, with the $4d$ sites constituting the majority sublattice, although the Mn moment is smaller in $4d$ than in $2b$ sites. The source of the strong uniaxial anisotropy and coercivity is the $4d$-site Mn.

We find evidence for a noncollinear deviation from the ferrimagnetic magnetic ground state in some samples, where the $2b$ moment has a soft intrinsic in-plane component. The noncollinear structure reflects both the easy-plane anisotropy at the $2b$ site and competing Mn-Mn exchange interactions. It cannot be explained solely by the difference in anisotropy at the two sites. Using x-ray absorption spectroscopies, we are able to determine the magnitude and direction of the spin and orbital magnetic moments on each site.

The noncollinear ground state is reminiscent of the magnetic ground state of α-Mn, but the Curie temperature of Mn_3Ga is much higher, and the material is suitable for applications requiring perpendicular thin films. This unusual magnetic order may find use in applications such as magnetic recording, spin-torque switching in thin-film devices, and generation of high-frequency radiation for which the relatively high spin polarization may be advantageous.

---

*rodek@tcd.ie

†Present address: Engineering physics department, Istanbul Medeniyet University, Goztepe Kadikoy/Istanbul, Turkey.

[1] D. D. Djayaprawira, K. Tsunekawa, M. Nagai, H. Maehara, S. Yamagata, N. Watanabe, S. Yuasa, Y. Suzuki, and K. Ando, Appl. Phys. Lett. **86**, 092502 (2005).

[2] W. H. Butler, X. G. Zhang, T. C. Schulthess, and J. M. MacLaren, Phys. Rev. B **63**, 054416 (2001).

[3] J. Mathon and A. Umerski, Phys. Rev. B **63**, 220403(R) (2001).

[4] S. Ikeda, K. Miura, H. Yamamoto, K. Mizunuma, H. D. Gan, M. Endo, S. Kanai, J. Hayakawa, F. Matsukura, and H. Ohno, Nat. Mater. **9**, 721 (2010).

[5] D. C. Worledge, G. Hu, D. W. Abraham, J. Z. Sun, P. L. Trouilloud, J. Nowak, S. Brown, M. C. Gaidis, E. J. O'Sullivan, and R. P. Robertazzi, Appl. Phys. Lett. **98**, 022501 (2011).

[6] H. D. Gan, H. Sato, M. Yamanouchi, S. Ikeda, K. Miura, R. Koizumi, F. Matsukura, and H. Ohno, Appl. Phys. Lett. **99**, 252507 (2011).

[7] T. Graf, C. Felser, and S. S. P. Parkin, Prog. Solid State Chem. **39**, 1 (2011).

[8] D. I. Bilc and P. Ghosez, Phys. Rev. B **83**, 205204 (2011).

[9] S. Chadov, X. Qi, J. Kübler, G. H. Fecher, C. Felser, and S. C. Zhang, Nat. Mater. **9**, 541 (2010).

[10] H. Lin, L. A. Wray, Y. Xia, S. Xu, S. Jia, R. J. Cava, A. Bansil, and M. Z. Hasan, Nat. Mater. **9**, 546 (2010).

[11] Y. Sakuraba, M. Hattori, M. Oogane, Y. Ando, H. Kato, A. Sakuma, T. Miyazaki, and H. Kubota, Appl. Phys. Lett. **88**, 192508 (2006).

[12] H.-x. Liu, Y. Honda, T. Taira, K.-i. Matsuda, M. Arita, T. Uemura, and M. Yamamoto, Appl. Phys. Lett. **101**, 132418 (2012).

[13] T. Iwase, Y. Sakuraba, S. Bosu, K. Saito, S. Mitani, and K. Takanashi, Appl. Phys. Express **2**, 063003 (2009).

[14]Y. Sakuraba, K. Izumi, T. Iwase, S. Bosu, K. Saito, K. Takanashi, Y. Miura, K. Futatsukawa, K. Abe, and M. Shirai, Phys. Rev. B **82**, 094444 (2010).

[15]H. Kurt, K. Rode, M. Venkatesan, P. Stamenov, and J. M. D. Coey, Phys. Rev. B **83**, 020405(R) (2011).

[16]H. Kurt, K. Rode, M. Venkatesan, P. Stamenov, and J. M. D. Coey, Phys. Status Solidi B **248**, 2338 (2011).

[17]B. Balke, G. H. Fecher, J. Winterlik, and C. Felser, Appl. Phys. Lett. **90**, 152504 (2007).

[18]J. Winterlik, B. Balke, G. H. Fecher, C. Felser, M. C. M. Alves, F. Bernardi, and J. Morais, Phys. Rev. B **77**, 054406 (2008).

[19]V. Briois, E. Fonda, S. Belin, L. Barthe, C. La Fontaine, F. Langlois, M. Ribbens, and F. Villain, in *UVX 2010-10e Colloque sur les Sources Cohérentes et Incohérentes UV, VUV et X; Applications et Développements Récents*, edited by A. Calisti, C. Mossé, and S. Ferri (EDP Sciences, Ile de Porquerolles, France, 2011), pp. 41–47.

[20]K. Wang, A. Chinchore, W. Lin, D. C. Ingram, A. R. Smith, A. J. Hauser, and F. Yang, J. Cryst. Growth **311**, 2265 (2009).

[21]K. M. Krishnan, Appl. Phys. Lett. **61**, 2365 (1992).

[22]J. J. Rehr, J. J. Kas, M. P. Prange, A. P. Sorini, Y. Takimoto, and F. Vila, C. R. Phys. **10**, 548 (2009).

[23]J. J. Rehr and R. C. Albers, Rev. Mod. Phys. **72**, 621 (2000).

[24]S. Chadov, J. Kiss, and C. Felser, Adv. Funct. Mater. **23**, 832 (2013).

[25]P. J. Webster, J. Phys. Chem. Solids **32**, 1221 (1971).

[26]A. T. Zayak, P. Entel, K. M. Rabe, W. A. Adeagbo, and M. Acet, Phys. Rev. B **72**, 054113 (2005).

[27]B. T. Thole, P. Carra, F. Sette, and G. van der Laan, Phys. Rev. Lett. **68**, 1943 (1992).

[28]P. Carra, B. T. Thole, M. Altarelli, and X. Wang, Phys. Rev. Lett. **70**, 694 (1993).

[29]M. Altarelli, Phys. Rev. B **47**, 597 (1993).

[30]M. Weinert, E. Wimmer, and A. J. Freeman, Phys. Rev. B **26**, 4571 (1982).

[31]E. Wimmer, H. Krakauer, M. Weinert, and A. J. Freeman, Phys. Rev. B **24**, 864 (1981).

[32]S. Blügel and G. Bihlmayer, in *Computional Nanoscience: Do it Yourself*, edited by J. Grotendorst, S. Blügel, and D. Marx (John von Neumann-Insitute für Computing, Forschungszentrum Jülich, 2006).

[33]C. Li, A. J. Freeman, H. J. F. Jansen, and C. L. Fu, Phys. Rev. B **42**, 5433 (1990).

[34]J. P. Perdew, K. Burke, and M. Ernzerhof, Phys. Rev. Lett. **77**, 3865 (1996).

[35]M. Alouani, J. M. Wills, and J. W. Wilkins, Phys. Rev. B **57**, 9502 (1998).

[36]N. Baadji, M. Alouani, and H. Dreyssé, Europhys. Lett. **87**, 27004 (2009).

[37]J. Kübler, J. Phys.: Condens. Matter **18**, 9795 (2006).

[38]A. R. Mackintosh and O. K. Anderson, *Electrons at the Fermi Surface*, Chap. 5 (Cambridge University Press, Cambridge, 1980), pp. 149–224.

[39]M. Weinert, R. E. Watson, and J. W. Davenport, Phys. Rev. B **32**, 2115 (1985).

[40]D. Hobbs, J. Hafner, and D. Spišák, Phys. Rev. B **68**, 014407 (2003).